JOURNAL OF PROPULSION AND POWER
Vol. 9, No. 4, July–Aug. 1993

Multigrid Calculation of Three-Dimensional Viscous Cascade Flows

A. Arnone*
University of Florence, Florence 50139, Italy
and
M.-S. Liou† and L. A. Povinelli‡
NASA Lewis Research Center, Cleveland, Ohio 44135

A three-dimensional code for viscous cascade flow prediction has been developed. The space discretization uses a cell-centered scheme with eigenvalue scaling to weigh the artificial dissipation terms. Computational efficiency of a four-stage Runge-Kutta scheme is enhanced by using variable coefficients, implicit residual smoothing, and a full-multigrid method. The Baldwin-Lomax eddy-viscosity model is used for turbulence closure. A zonal, nonperiodic grid is used to minimize mesh distortion in and downstream of the throat region. Applications are presented for an annular vane with and without end wall contouring, and for a large-scale linear cascade. The calculation is validated by comparing with experiments and by studying grid dependency.

Introduction

IMPROVING efficiency and specific work while reducing weight, cost, and number of components and maintaining a good level of performance in a wide range of operational conditions is the goal of turbomachinery design. The last decade has seen an impressive evolution both in the understanding and in the simulation of flow features. In this process computational fluid dynamics (CFD) is playing a more and more important role. In turbomachinery applications, modern components operate under very complex three-dimensional flow conditions, and further improvement of performance requires detailed knowledge of the flow structure. Particularly, the need to predict off-design conditions, secondary flows, and heat transfer forces us to look at viscous models. Even if a two-dimensional or quasi-three-dimensional analysis is very useful, three-dimensional simulation will be the basic tool in the design of the next generation of turbomachinery. The real flow inside a turbomachine is unsteady and dominated by rotor-stator interactions and wake effects. However, the time-accurate simulation of an entire turbine or compressor is beyond the capability of current computers. On the contrary, a steady, viscous, blade-row analysis is now beginning to be feasible for designers, although much effort is still needed to improve accuracy and to reduce the computational cost. Some important examples of three-dimensional viscous cascade flow predictions are in Refs. 1–7.

In 1988, we started a research project on viscous cascade flow simulation. During this work, we developed the TRAF2D code (transonic flow 2-dimensional).[8,9] This code is capable of solving two-dimensional viscous cascade flows using H-type or C-type grids and of predicting heat transfer effects. In this article the procedure is extended to the three-dimensional case (TRAF3D). Particular attention has been dedicated to aspects which are important for the designer, such as accuracy, computational cost, and the correct prediction of pressure, exit angles, and loss coefficients.

As for accuracy, a new kind of elliptically generated C-type grid is stacked in three dimensions. The removal of periodicity on the wake allows the grid to be only slightly distorted, even for cascades having a large camber or a high stagger angle. This allows us to pick up details of the throat flow with a reasonable number of grid points. In addition, a very low level of artificial dissipation is guaranteed by eigenvalues scaling, which is a three-dimensional extension of the one proposed by Martinelli[10] and Swanson and Turkel.[11]

As for efficiency, the Reynolds-averaged Navier-Stokes equations are solved using a Runge-Kutta scheme in conjunction with accelerating techniques. Variable-coefficient implicit residual smoothing, as well as the full approximation storage (FAS) multigrid scheme of Brandt and Jameson have been used in the TRAF3D code. Those accelerating strategies are implemented in conjunction with grid refinement to get a "full multigrid method." The two-layer eddy-viscosity model of Baldwin and Lomax[12] is used for the turbulence closure.

The capability of the code is shown by comparing the computed results to experiments for the Goldman annular vane with and without end-wall contouring, and for the low-speed Langston linear cascade. For the case of the vane, a grid-dependency analysis is presented.

By using the accelerating strategies, detailed, viscous three-dimensional solutions on a grid with nearly a half-million points can be obtained in less than 1 h on a modern supercomputer such as a Cray Y-MP.

Governing Equations

Let ρ, u, v, w, p, T, E, and H denote density, the absolute velocity components in the x, y, and z Cartesian directions, pressure, temperature, specific total energy, and specific total enthalpy, respectively. The three-dimensional, unsteady, Reynolds-averaged Navier-Stokes equations, neglecting body forces and heat sources, can be written for a fixed-blade passage in conservative form in a curvilinear coordinate system ξ, η, ζ as

$$\frac{\partial(J^{-1}Q)}{\partial t} + \frac{\partial F}{\partial \xi} + \frac{\partial G}{\partial \eta} + \frac{\partial H}{\partial \zeta} = \frac{\partial F_v}{\partial \xi} + \frac{\partial G_v}{\partial \eta} + \frac{\partial H_v}{\partial \zeta} \quad (1)$$

Presented as Paper 91-3238 at the AIAA 9th Applied Aerodynamics Conference, Baltimore, MD, Sept. 23–25, 1991; received Oct. 24, 1991; revision received Feb. 21, 1993; accepted for publication Feb. 25, 1993.

*Assistant Professor, Department of Energy Engineering, Via S. Marta, 3.
†Senior Scientist, Internal Fluid Mechanics Division. Member AIAA.
‡Deputy Chief, Internal Fluid Mechanics Division. Fellow AIAA.

where

$$Q = \begin{bmatrix} \rho \\ \rho u \\ \rho v \\ \rho w \\ \rho E \end{bmatrix}, \quad F = J^{-1} \begin{bmatrix} \rho U \\ \rho u U + \xi_x p \\ \rho v U + \xi_y p \\ \rho w U + \xi_z p \\ \rho H U \end{bmatrix} \tag{2}$$

$$G = J^{-1} \begin{bmatrix} \rho V \\ \rho u V + \eta_x p \\ \rho v V + \eta_y p \\ \rho w V + \eta_z p \\ \rho H V \end{bmatrix}, \quad H = J^{-1} \begin{bmatrix} \rho W \\ \rho u W + \zeta_x p \\ \rho v W + \zeta_y p \\ \rho w W + \zeta_z p \\ \rho H W \end{bmatrix}$$

The contravariant velocity components of Eq. (2) are written as

$$U = \xi_x u + \xi_y v + \xi_z w, \quad V = \eta_x u + \eta_y v + \eta_z w$$
$$W = \zeta_x u + \zeta_y v + \zeta_z w \tag{3}$$

and the transformation metrics are defined by

$$\begin{aligned} \xi_x &= J(y_\eta z_\zeta - y_\zeta z_\eta), \quad \xi_y = J(z_\eta x_\zeta - z_\zeta x_\eta), \quad \xi_z = J(x_\eta y_\zeta - x_\zeta y_\eta) \\ \eta_x &= J(y_\zeta z_\xi - y_\xi z_\zeta), \quad \eta_y = J(z_\zeta x_\xi - z_\xi x_\zeta), \quad \eta_x = J(x_\zeta y_\xi - x_\xi y_\zeta) \\ \zeta_x &= J(y_\xi z_\eta - z_\xi y_\eta), \quad \zeta_y = J(z_\xi x_\eta - x_\xi z_\eta), \quad \zeta_z = J(x_\xi y_\eta - y_\xi x_\eta) \end{aligned} \tag{4}$$

where the Jacobian of the transformation J is

$$J^{-1} = x_\xi y_\eta z_\zeta + x_\eta y_\zeta z_\xi + x_\zeta y_\xi z_\eta - x_\xi y_\zeta z_\eta - x_\eta y_\xi z_\zeta - x_\zeta y_\eta z_\xi \tag{5}$$

The viscous flux terms are assembled in the form

$$F_v = J^{-1} \begin{bmatrix} 0 \\ \xi_x \tau_{xx} + \xi_y \tau_{xy} + \xi_z \tau_{xz} \\ \xi_x \tau_{yx} + \xi_y \tau_{yy} + \xi_z \tau_{yz} \\ \xi_x \tau_{zx} + \xi_y \tau_{zy} + \xi_z \tau_{zz} \\ \xi_x \beta_x + \xi_y \beta_y + \xi_z \beta_z \end{bmatrix}$$

$$G_v = J^{-1} \begin{bmatrix} 0 \\ \eta_x \tau_{xx} + \eta_y \tau_{xy} + \eta_z \tau_{xz} \\ \eta_x \tau_{yx} + \eta_y \tau_{yy} + \eta_z \tau_{yz} \\ \eta_x \tau_{zx} + \eta_y \tau_{zy} + \eta_z \tau_{zz} \\ \eta_x \beta_x + \eta_y \beta_y + \eta_z \beta_z \end{bmatrix} \tag{6}$$

$$H_v = J^{-1} \begin{bmatrix} 0 \\ \zeta_x \tau_{xx} + \zeta_y \tau_{xy} + \zeta_z \tau_{xz} \\ \zeta_x \tau_{yx} + \zeta_y \tau_{yy} + \zeta_z \tau_{yz} \\ \zeta_x \tau_{zx} + \zeta_y \tau_{zy} + \zeta_z \tau_{zz} \\ \zeta_x \beta_x + \zeta_y \beta_y + \zeta_z \beta_z \end{bmatrix}$$

where

$$\begin{aligned} \tau_{xx} &= 2\mu u_x + \lambda(u_x + v_y + w_z) \\ \tau_{yy} &= 2\mu v_y + \lambda(u_x + v_y + w_z) \\ \tau_{zz} &= 2\mu w_z + \lambda(u_x + v_y + w_z) \\ \tau_{xy} &= \tau_{yx} = \mu(u_y + v_x) \\ \tau_{xz} &= \tau_{zx} = \mu(u_2 + w_x) \\ \tau_{yz} &= \tau_{zy} = \mu(v_z + w_y) \\ \beta_x &= u\tau_{xx} + v\tau_{xy} + w\tau_{xz} + kT_x \\ \beta_y &= u\tau_{yx} + v\tau_{yy} + w\tau_{yz} + kT_y \\ \beta_z &= u\tau_{zx} + v\tau_{zy} + w\tau_{zz} + kT_z \end{aligned} \tag{7}$$

and the Cartesian derivatives of Eq. (7) are expressed in terms of ξ, η, and ζ derivatives using the chain rule, i.e.

$$u_x = \xi_x u_\xi + \eta_x u_\eta + \zeta_x u_\zeta \tag{8}$$

The pressure is obtained from the equation of state

$$p = \rho RT \tag{9}$$

According to the Stokes hypothesis, λ is taken to be $-2\mu/3$, and a power law is used to determine the molecular coefficient of viscosity μ as function of temperature. The eddy-viscosity hypothesis is used to account for the effect of turbulence. The molecular viscosity μ and the molecular thermal conductivity k are replaced with

$$\mu = \mu_l + \mu_t \tag{10}$$

$$k = c_p[(\mu/Pr)_l + (\mu/Pr)_t] \tag{11}$$

where c_p is the specific heat at constant pressure, Pr is the Prandtl number, and the subscripts l and t refer to laminar and turbulent, respectively. The turbulent quantities μ_t and Pr_t are computed using the two-layer mixing length model of Baldwin and Lomax.[12] The contribution of the eddy-viscosity is computed separately in the blade-to-blade direction η and in the spanwise direction ζ. The inverse of the square of the wall distances d is then used to compute the resulting eddy-viscosity

$$f = \frac{(1/d_\eta^2)}{[(1/d_\eta^2) + (1/d_\zeta^2)]} \tag{12}$$

$$\mu_t = f(\mu_t)_\eta + (1 - f)(\mu_t)_\zeta \tag{13}$$

The transitional criteria of Baldwin and Lomax is adopted on the airfoil surface while on the end walls, the shear layer is assumed to be fully turbulent from the inlet boundary.

Spatial Discretization

Traditionally, using a finite volume approach, the governing equations are discretized in space starting from an integral formulation and without any intermediate mapping. The transformation metrics of Eq. (4) can then be associated with the projections of the face areas as the contravariant components of Eq. (3) can be related to the normal components of the velocity. In the present work, due to the large use of eigenvalues and curvilinear quantities, we found it more convenient to map the Cartesian space (x, y, z) in a generalized curvilinear one (ξ, η, ζ). In the curvilinear system, the equation of motion [Eq. (1)] can easily be rewritten in integral form by means of Green's theorem, and the metric terms are handled following the standard finite volume formulation. The computational domain is divided into hexahedrons and the transformation metrics are evaluated so that the projected areas of the cell faces are given by the ratio of the appropriate metric derivatives to the Jacobian ones, i.e., ξ_x/J is the projection onto the x axis of a cell face at a fixed ξ location. A cell-centered scheme is used to store the flow variables. On each cell face the convective and diffusive fluxes are calculated after computing the necessary flow quantities at the face center. Those quantities are obtained by a simple averaging of adjacent cell-center values of the dependent variables.

Boundary Conditions

In cascade calculations we have four different types of boundaries: 1) inlet, 2) outlet, 3) solid walls, and 4) periodicity. At the inlet, the presence of boundary layers (on hub and tip end walls) is accounted for by giving a total pressure and a total temperature profile whose distribution simulates the experimental one. According to the theory of character-

istics, the flow angles, total pressure, total temperature, and isentropic relations are used at the subsonic-axial inlet, while the outgoing Riemann invariant is taken from the interior. At the subsonic-axial outlet, the average value of the static pressure at the hub is prescribed and the density and components of velocity are extrapolated together with the circumferential distribution of pressure. The radial equilibrium equation is used to determine the spanwise distribution of the static pressure. On the solid walls, the pressure is extrapolated from the interior points, and the no-slip condition and the temperature condition are used to compute density and total energy. For the calculations presented in this article, all the walls have been assumed to be adiabatic.

Cell-centered schemes are generally implemented using phantom cells to handle the boundaries. The periodicity from blade passage to blade passage is, therefore, easily overimposed by setting periodic phantom cell values. On the boundaries where the grid is not periodic, the phantom cells overlap the real ones. Linear interpolations are then used to compute the value of the dependent variables in phantom cells.

Artificial Dissipation

In viscous calculations, dissipating properties are present due to diffusive terms. Away from the shear-layer regions, the physical diffusion is generally not sufficient to prevent the odd-even point decoupling of centered schemes. Thus, to maintain stability and to prevent oscillations near shocks or stagnation points, artificial dissipation terms are also included in the viscous calculations. Equation (1) is written in semi-discrete form as

$$\frac{\partial Q}{\partial t} + C(Q) - D(Q) = 0 \tag{14}$$

where the discrete operator C accounts for the physical convective and diffusive terms, while D is the operator for the artificial dissipation. The artificial dissipation model used in this article is basically the one originally introduced by Jameson et al.[13] In order to minimize the amount of artificial diffusion inside the shear layer, the eigenvalues scaling of Martinelli[10] and Swanson and Turkel[11] have been used to weight these terms. The quantity $D(Q)$ in Eq. (14) is defined as

$$D(Q) = (D_\xi^2 - D_\xi^4 + D_\eta^2 - D_\eta^4 + D_\zeta^2 - D_\zeta^4)Q \tag{15}$$

where, e.g., in the ξ curvilinear coordinates we have

$$\begin{aligned} D_\xi^2 Q &= \nabla_\xi[\Lambda_{i+1/2,j,k}\varepsilon^{(2)}_{i+1/2,j,k}]\Delta_\xi Q_{i,j,k} \\ D_\xi^4 Q &= \nabla_\xi[\Lambda_{i+1/2,j,k}\varepsilon^{(4)}_{i+1/2,j,k}]\Delta_\xi \nabla_\xi \Delta_\xi Q_{i,j,k} \end{aligned} \tag{16}$$

i, j, k are indices associated with the ξ, η, ζ directions, and ∇_ξ, Δ_ξ are forward and backward difference operators in the ξ direction. The variable scaling factor Λ is defined for the three-dimensional case as

$$\Lambda_{i+1/2,j,k} = \tfrac{1}{2}[(\Lambda_\xi)_{i,j,k} + (\Lambda_\xi)_{i+1,j,k}] \tag{17}$$

where

$$\Lambda_\xi = \Phi_\xi \lambda_\xi \tag{18}$$

The definition of the coefficient Φ has been extended to the three-dimensional case as follows:

$$\begin{aligned} \Phi_\xi &= 1 + (\lambda_\eta/\lambda_\xi)^\sigma + (\lambda_\zeta/\lambda_\xi)^\sigma \\ \Phi_\eta &= 1 + (\lambda_\xi/\lambda_\eta)^\sigma + (\lambda_\zeta/\lambda_\eta)^\sigma \\ \Phi_\zeta &= 1 + (\lambda_\xi/\lambda_\zeta)^\sigma + (\lambda_\eta/\lambda_\zeta)^\sigma \end{aligned} \tag{19}$$

where λ_ξ, λ_η, and λ_ζ are the scaled spectral radii of the flux Jacobian matrices for the convective terms

$$\begin{aligned} \lambda_\xi &= |U| + a\sqrt{\xi_x^2 + \xi_y^2 + \xi_z^2} \\ \lambda_\eta &= |V| + a\sqrt{\eta_x^2 + \eta_y^2 + \eta_z^2} \\ \lambda^\zeta &= |W| + a\sqrt{\zeta_x^2 + \zeta_y^2 + \zeta_z^2} \end{aligned} \tag{20}$$

and a is the speed of sound. The exponent σ is generally defined by $0 < \sigma \leq 1$, and for two-dimensional applications, a value of $\frac{2}{3}$ gives satisfactory results. In three-dimensional cascade flow calculations, we generally have highly stretched meshes in two directions near corners. We found that $\sigma = 0.4$ introduces enough scaling without compromising the robustness. The coefficients $\varepsilon^{(2)}$ and $\varepsilon^{(4)}$ use the pressure as a sensor for shocks and stagnation points, and are defined as follows:

$$\varepsilon^{(2)}_{i+1/2,j,k} = k^{(2)} \max(\nu_{i-1,j,k}, \nu_{i,j,k}, \nu_{i+1,j,k}, \nu_{i+2,j,k}) \tag{21}$$

$$\nu_{i,j,k} = \left| \frac{p_{i-1,j,k} - 2\,p_{i,j,k} + p_{i+1,j,k}}{p_{i-1,j,k} + 2\,p_{i,j,k} + p_{i+1,j,k}} \right| \tag{22}$$

$$\varepsilon^{(4)}_{i+1/2,j,k} = \max\{0, [K^{(4)} - \varepsilon^{(2)}_{i+1/2,j,k}]\} \tag{23}$$

where typical values for the constants $K^{(2)}$ and $K^{(4)}$ are $\frac{1}{2}$ and $\frac{1}{64}$, respectively. For the remaining directions η and ζ, the contribution of dissipation is defined in a similar way. The computation of the dissipating terms is carried out in each coordinate direction as the difference between first- and third-difference operators. Those operators are set to zero on solid walls in order to reduce the global error on the conservation property and to prevent the presence of undamped modes.[11,14,15]

Time-Stepping Scheme

The system of the differential Eq. (14) is advanced in time using an explicit four-stage Runge-Kutta scheme until the steady-state solution is reached. A hybrid scheme is implemented, where, for economy, the viscous terms are evaluated only at the first stage and then frozen for the remaining stages. If n is the index associated with time, we will write it in the form

$$\begin{aligned} Q^{(0)} &= Q^n \\ Q^{(1)} &= Q^{(0)} + \alpha_1 R[Q^{(0)}] \\ Q^{(2)} &= Q^{(0)} + \alpha_2 R[Q^{(1)}] \\ Q^{(3)} &= Q^{(0)} + \alpha_3 R[Q^{(2)}] \\ Q^{(4)} &= Q^{(0)} + \alpha_4 R[Q^{(3)}] \\ Q^{n+1} &= Q^{(4)} \\ \alpha_1 = \tfrac{1}{4}, &\quad \alpha_2 = \tfrac{1}{3}, \quad \alpha_3 = \tfrac{1}{2}, \quad \alpha_4 = 1 \end{aligned} \tag{24}$$

where the residual $R(Q)$ is defined by

$$R(Q) = \Delta t J[C(Q) - D(Q)] \tag{25}$$

Good, high-frequency damping properties, important for the multigrid process, have been obtained by performing two evaluations of the artificial dissipating terms, at the first and second stages. It is worthwhile to notice that, in the Runge-Kutta time-stepping schemes, the steady-state solution is independent of the time step; therefore, this stepping is particularly amenable to convergence acceleration techniques.

It is important to notice that from the definition of residual of Eq. (25), variable scaling, and time steps of Eqs. (26–28), it results that the artificial dissipation is scaled with a factor

proportional to the ratio between the global time step and the inviscid time step. Close to solid walls, the grid volume is very small and viscous time-step limitation is dominant. The ratio of the time step over the inviscid one becomes very small and most of the artificial dissipation is removed.

Acceleration Techniques

In order to reduce the computational cost, four techniques are employed to speed up convergence to the steady-state solution. These techniques 1) local time stepping, 2) residual smoothing, 3) multigrid, and 4) grid refinement are separately described in the following.

Local Time Stepping

For steady-state calculations with a time-marching approach, a faster expulsion of disturbances can be achieved by locally using the maximum available time step. In the present work, the local time-step limit Δt is computed accounting for both the convective (Δt_c) and diffusive (Δt_d) contributions as follows:

$$\Delta t = c_0 \left(\frac{\Delta t_c \Delta t_d}{\Delta t_c + \Delta t_d} \right) \tag{26}$$

where c_0 is a constant usually taken to be the Courant-Friedrichs-Lewy (CFL) number. Specifically, for the inviscid and viscous time step we used

$$\Delta t_c = [1/(\lambda_\xi + \lambda_\eta + \lambda_\zeta)] \tag{27}$$

$$\Delta t_d = [1/K_t(\gamma\mu/\rho Pr)J^2(S_\eta^2 S_\xi^2 + S_\xi^2 S_\zeta^2 + S_\xi^2 S_\eta^2)] \tag{28}$$

where γ is the specific heat ratio and

$$S_\xi^2 = x_\xi^2 + y_\xi^2 + z_\xi^2, \quad S_\eta^2 = x_\eta^2 + y_\eta^2 + z_\eta^2$$
$$S_\zeta^2 = x_\zeta^2 + y_\zeta^2 + z_\zeta^2 \tag{29}$$

K_t being a constant whose value has been set equal to 2.5 based on numerical experiments.

Residual Smoothing

An implicit smoothing of residuals is used to extend the stability limit and the robustness of the basic scheme. This technique was first introduced by Lerat[16] in 1979 in conjunction with Lax-Wendroff-type schemes. Later, in 1983, Jameson[17] implemented it on the Runge-Kutta stepping scheme. In three dimensions we carried out the residual smoothing in the form

$$(1 - \beta_\xi \nabla_\xi \Delta_\xi)(1 - \beta_\eta \nabla_\eta \Delta_\eta)(1 - \beta_\zeta \nabla_\zeta \Delta_\zeta)\bar{R} = R \tag{30}$$

where the residual R includes the contribution of the variable time step and is defined by Eq. (25), and $\bar{R}$ is the residual after a sequence of smoothing in the ξ, η, and ζ directions with coefficients β_ξ, β_η, and β_ζ.

For viscous calculations on highly stretched meshes, the variable coefficient formulations of Martinelli[10] and Swanson[11] have proven to be robust and reliable. In this article, the expression for the variable coefficients β of Eq. (30) has been modified to be used in three dimensions as follows:

$$\beta_\xi = \max\left\{0, \frac{1}{4}\left[\left(\frac{\text{CFL}}{\text{CFL}^*}\frac{\lambda_\xi}{\lambda_\xi + \lambda_\eta + \lambda_\zeta}\Phi_\xi\right)^2 - 1\right]\right\}$$
$$\beta_\eta = \max\left\{0, \frac{1}{4}\left[\left(\frac{\text{CFL}}{\text{CFL}^*}\frac{\lambda_\eta}{\lambda_\xi + \lambda_\eta + \lambda_\zeta}\Phi_\eta\right)^2 - 1\right]\right\} \tag{31}$$
$$\beta_\zeta = \max\left\{0, \frac{1}{4}\left[\left(\frac{\text{CFL}}{\text{CFL}^*}\frac{\lambda_\zeta}{\lambda_\xi + \lambda_\eta + \lambda_\zeta}\Phi_\zeta\right)^2 - 1\right]\right\}$$

where the coefficients Φ_x, Φ_y, and Φ_z are the ones defined in Eq. (19), and CFL, and CFL* are the Courant numbers of the smoothed and unsmoothed scheme, respectively. For the hybrid four-stage scheme we used CFL = 5, and CFL* = 2.5.

Multigrid

This technique was developed in the beginning of the 1970s for the solution of elliptic problems[18] and was later extended to time-dependent formulations.[19,20] The basic idea is to introduce a sequence of coarser grids and to use them to speed up the propagation of the fine grid corrections, resulting in a faster expulsion of disturbances. In this work we used the FAS schemes of Brandt[18] and Jameson.[20]

Coarser, auxiliary meshes are obtained by doubling the mesh spacing and the solution is defined on them using a rule which conserves mass, momentum, and energy

$$[J^{-1}Q^{(0)}]_{2h} = \sum (J^{-1}Q)_h \tag{32}$$

where the subscripts refer to the grid spacing, and the sum is over the eight cells which compose the $2h$ grid cell. Note that this definition coincides with the one used by Jameson when the reciprocal of the Jacobians are replaced with the cell volumes. To respect the fine grid approximation, forcing functions P are defined on the coarser grids and added to the governing equations. So, after the initialization of Q_{2h} using Eq. (32), forcing functions P_{2h} are defined as

$$P_{2h} = \sum R_h(Q_h) - R_{2h}(Q_{2h}^{(0)}) \tag{33}$$

and added to the residuals R_{2h} to obtain the value R_{2h}^* which is then used for the stepping scheme:

$$R_{2h}^* = R_{2h}(Q_{2h}) + P_{2h} \tag{34}$$

This procedure is repeated on a succession of coarser grids and the corrections computed on each coarse grid are transferred back to the finer one by bilinear interpolations.

A V-type cycle with subiterations is used as a multigrid strategy. The process is advanced from the fine grid to the coarser one without any intermediate interpolation, and when the coarser grid is reached, corrections are passed back. One Runge-Kutta step is performed on the h grid, two on the $2h$ grid, and three on all the coarser grids. It is our experience in cascade flow calculations that subiterations increase the robustness of the multigrid.

For viscous flows with very low Reynolds number or strong separation, it is important to compute the viscous terms on the coarse grids, too. The turbulent viscosity is evaluated only on the finest grid level and then interpolated on coarse grids.

On each grid, the boundary conditions are treated in the same way and updated at every Runge-Kutta stage. For economy, the artificial dissipation model is replaced on the coarse grids with constant coefficient second-order differences.

The interpolations of the corrections introduce high-frequency errors. In order to prevent those errors from being reflected in the eddy viscosity, turbulent quantities are updated after performing the stepping on the fine grid. On coarse grids, the turbulent viscosity is evaluated by averaging the surrounding fine grid values.

Grid Refinement

A grid refinement strategy is used to provide a cost-effective initialization of the fine grid solution. This strategy is implemented in conjunction with multigrid to obtain a full multigrid (FMG) procedure. With the FMG method, the solution is initialized on a coarser grid of the basic grid sequence and iterated a prescribed number of cycles of the FAS scheme. The solution is then passed, by bilinear interpolations, onto the next, finer grid and the process is repeated until the finest

grid level is reached. In this article we have introduced three levels of refinement with two, three, and four grids, respectively.

Computational Grid

The three-dimensional grids are obtained by stacking two-dimensional grids generated on the blade-to-blade surface (ξ, η plane). In the blade-to-blade projection, the grids are nonperiodic C-type ones and are elliptically generated, controlling the grid spacing and orientation at the wall. The C-type structure has been chosen to model the blunt leading edge typical of turbine blading. The problem of grid skewness due to high stagger or large camber is addressed by allowing the grid to be nonperiodic on the wake. This grid structure, recently introduced by the authors[9] for two-dimensional applications, has proven to be effective in turbomachinery applications.

In the spanwise direction (ζ) a standard H-type structure has been adopted. Near the hub and tip walls, geometric stretching is used for a specified number of grid points, after which the spanwise spacing remains constant.

Applications and Discussion

As applications of the procedure that has been described above, we used the TRAF3D code to predict the flow in an annular and linear cascade. The annular cascade is the one tested by Goldman and Seasholtz,[21,22] and experiments are available for configurations both with and without end-wall contouring. The inlet boundary layer for this case is quite thin and the secondary flows are not extremely pronounced. On the contrary, the large-scale linear cascade of Langston[23,24] is

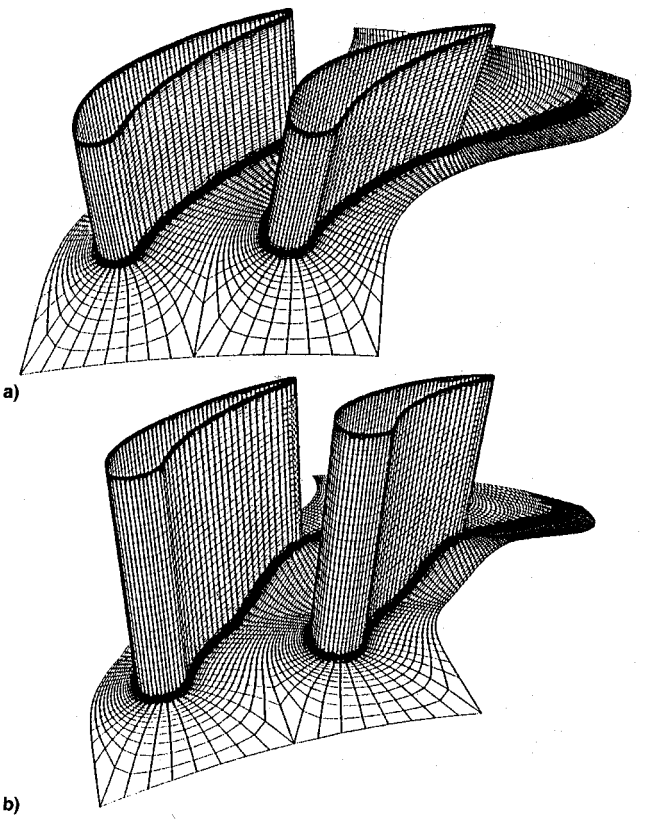

Fig. 1 177 × 33 × 65 Computational grids for the Goldman annular vanes with and without contoured end walls: a) without contoured end wall, b) with contoured end wall.

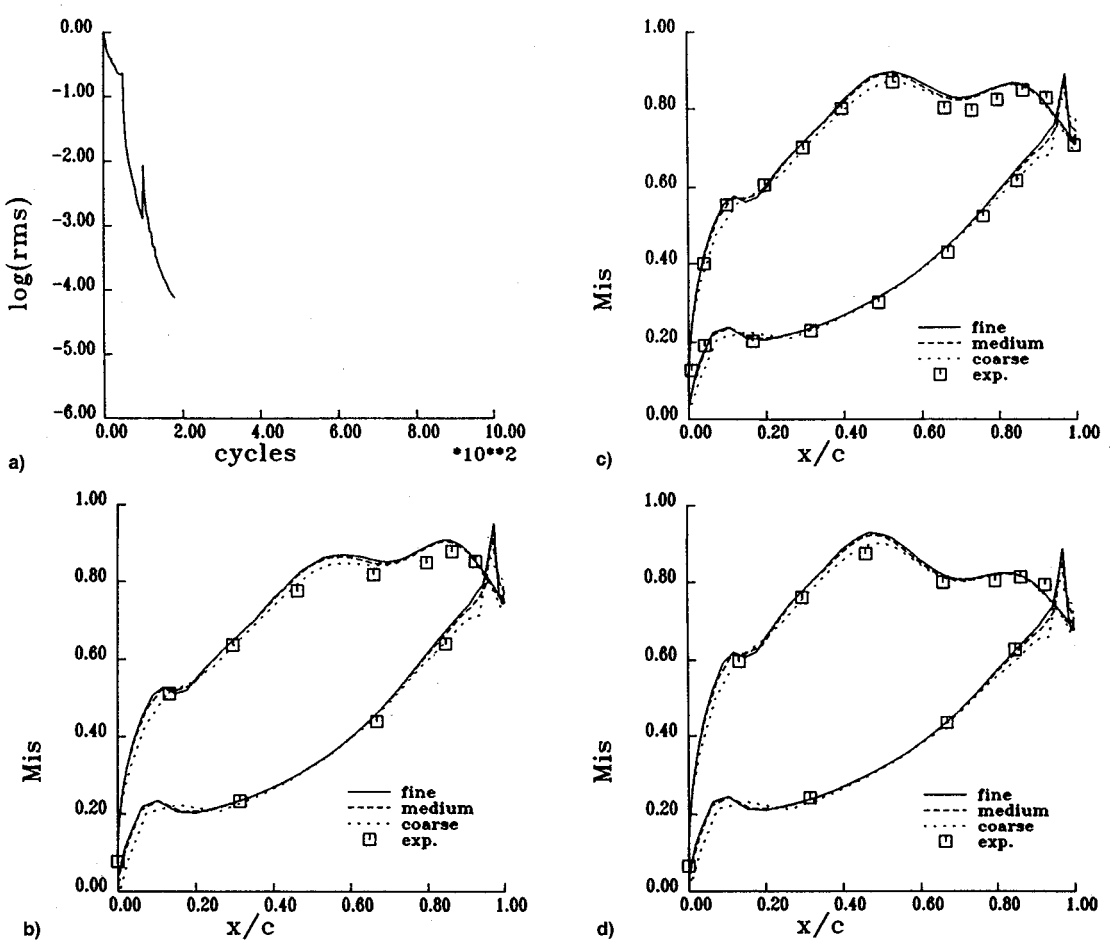

Fig. 2 Goldman annular vane without contoured end wall: a) convergence history, b) isentropic Mach number distribution near hub, c) isentropic Mach number distribution at midspan, and d) isentropic Mach number distribution near tip.

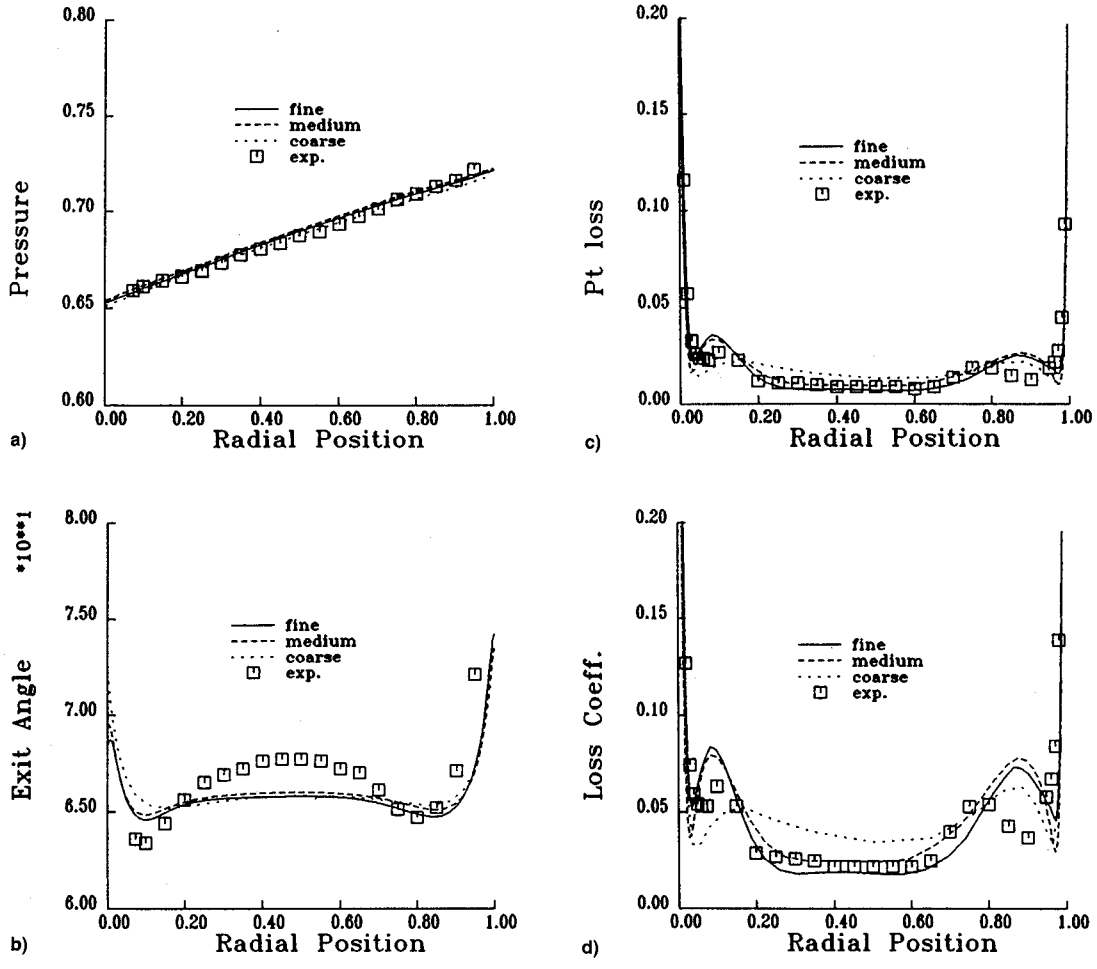

Fig. 3 Goldman annular vane without contoured end wall. After-mixed spanwise distribution of pressure, exit angle, and loss coefficients at $\frac{1}{3}$ axial chord away from trailing edge: a) pressure, b) exit angle, c) total pressure loss, and d) energy loss coefficient.

a nice test case to investigate the code's capability of predicting the three-dimensional features of the flow.

Calculations for these three blade passages will be presented in this section along with a grid sensitivity study.

Goldman Annular Vane

This annular vane was tested by Goldman[21] with laser anemometer measurements. Pressure distribution in the blade passage, and details of the exit losses and angle spanwise variations made this test very interesting for code assessment.

In a previous work[9] we carried out a two-dimensional grid dependency study in order to figure out the mesh requirements necessary to obtain a space-converged calculation, especially for skin friction and heat transfer predictions. Those results can be extrapolated to the three-dimensional case, but the resulting number of grid points is quite large, nearly a half-million points. In three-dimensional applications, the memory and time requirements can be large, even for a modern supercomputer, so a grid dependency study can be useful in optimizing the mesh size. We introduced three grids of 97 $\times$ 17 $\times$ 25, 127 $\times$ 25 $\times$ 49, and 177 $\times$ 33 $\times$ 65 grid points, respectively. The fine mesh spacing at the wall is 2×10^{-4} axial chord in the blade-to-blade direction and 5×10^{-4} in the spanwise one. Using those spacings, the y^+ at the wall is roughly less than two when the exit Reynolds number is about one million. On the medium and coarse grids, the wall spacings are two times and four times the fine grid ones, respectively. On the three meshes there are 33, 49, and 65 points, respectively, on the suction surface of the airfoil. A three-dimensional view of the fine grid for the Goldman cascade without end-wall contouring is given in Fig. 1a. The low level of skewness obtained by stacking nonperiodic C-type grids is evident.

The convergence of the rms of the residuals of the continuity equation is given in Fig. 2a. This calculation refers to the fine mesh (380,000 grid points) and requires about 45 min on the Cray Y-MP. If we assume we have reached a good level of convergence when the residuals have dropped four decades, the medium mesh (156,000 grid points) takes 15 min, while about 6 min are needed for the coarse mesh calculation (41,000 grid points).

For this test case, the inlet flow is axial and the exit isentropic Mach number at the hub is about 0.809. Figures 2b–d show the experimental and computed isentropic surface Mach number distribution near the hub, at midspan, and near the tip. All the grids correctly predict the distribution, the slight underestimation of the coarse grid with respect to the medium and fine ones is mostly due to the higher level of predicted losses.

Goldman[21] measured the spanwise distributions of the after-mixed pressure, exit flow angle, total pressure loss coefficient, and energy loss coefficient at $\frac{1}{3}$ axial chord away from the trailing edge. The predicted distribution of these quantities is compared to experiments in Fig. 3. Overall, the agreement is very good. The radial distribution of the static pressure is accurately reproduced (see Fig. 3a), while the exit angle is qualitatively the same on all the grids, but with a smoother distribution with respect to experiments (Fig. 3b). From the plots of total pressure and energy loss coefficients of Figs. 3c and 3d we can draw some interesting conclusions. In the coarse grid, with only 25 points in the hub-to-tip direction, the distribution of the losses is only roughly captured. We need at

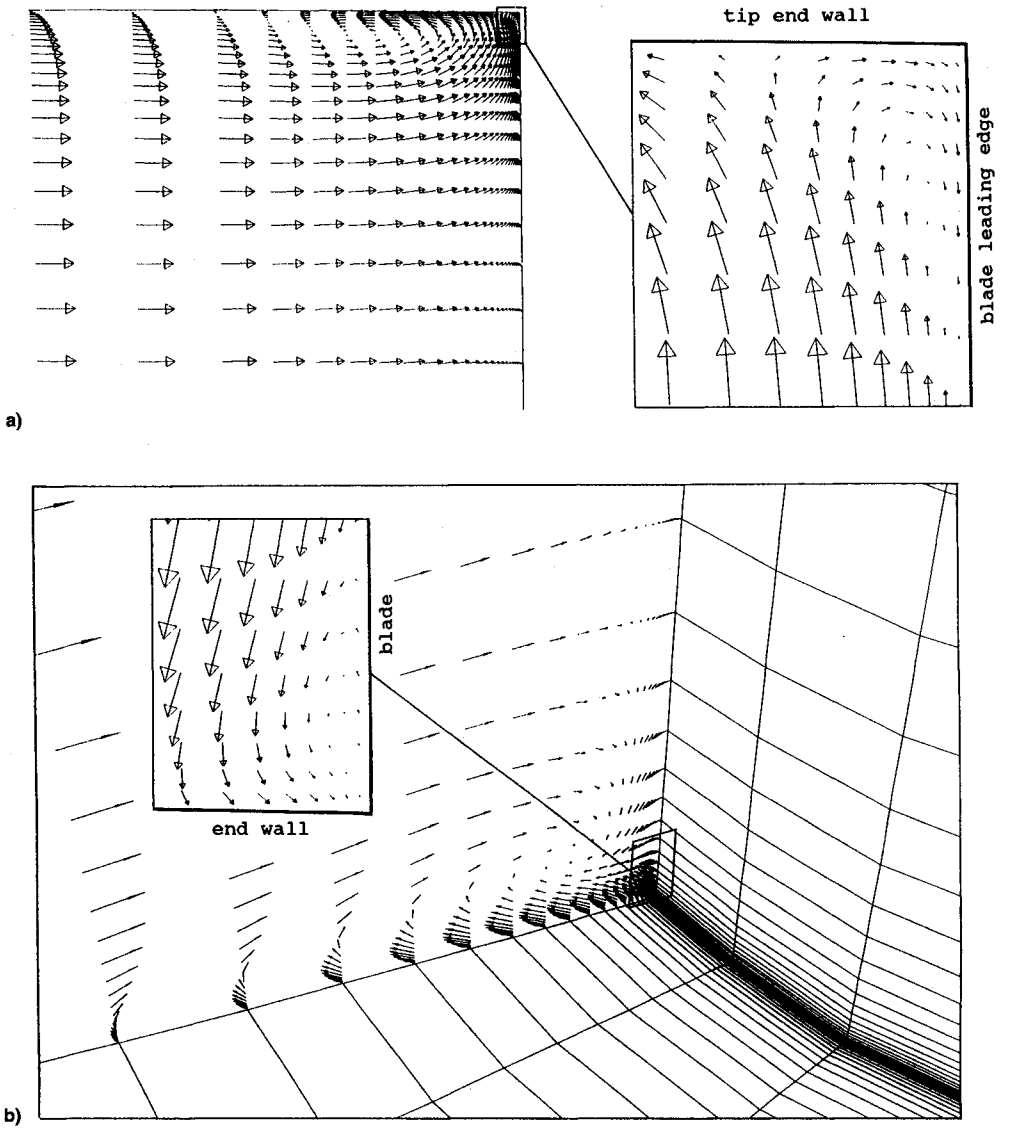

Fig. 4 Details of the horseshoe vortices near tip and hub: a) horseshoe vortex and counter-rotating corner vortex near tip, b) horseshoe vortex and counter-rotating corner vortex near hub.

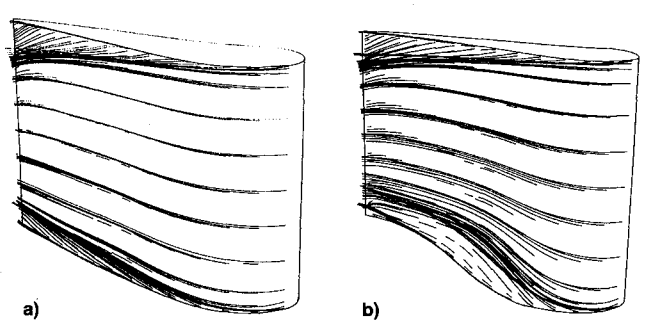

Fig. 5 Particle traces on the suction side of the Goldman annular vane: a) noncontoured end wall, b) contoured end wall.

least 49 points to have a spanwise loss prediction which is nearly space-converged. Coarse grid losses are also twice as large as the experiment at midspan, thus confirming the indication of the two-dimensional analysis[9] which suggested the use of y^+ near the unity. Both the medium and fine grids predict the losses well, except near the tip, where the boundary layer is thicker. The kink in the losses is computed closer to the wall than experiments indicate.

The position of the horseshoe vortices near the hub and tip is given in Fig. 4. The enlargements show the counter-rotating corner vortices.

The liftoff of the passage vortex on the suction side of the airfoil is evident from the particle trace near the wall of Fig. 5a. The effect is more pronounced near the tip because of the thicker inlet boundary layer.

Goldman Annular Vane with Contoured End Wall

Figure 1b shows the 177 × 33 × 65 computational mesh for the Goldman vane with an s-shaped contoured end wall at the hub after midchord. Some details of the calculation for this case are summarized in Figs. 5b and 6. The exit isentropic Mach number at the hub is now about 0.695. The computed surface isentropic Mach number agrees well with experiments[22] near the hub, at midspan, and near the tip. On the hub, the presence of the contoured end wall causes a stronger pressure gradient between pressure and suction sides, resulting in a stronger liftoff of streamlines on the suction side as shown by the simulated oil flow-trace of Fig. 5b.

Langston Low-Speed Linear Cascade

Langston et al.,[23] in 1976, made detailed measurements in a low-speed, large-scale plane turbine cascade. The work included experimental visualizations of the three-dimensional nature of the flow. The flow exhibits important three-dimensional separation on both airfoil surface and end wall.

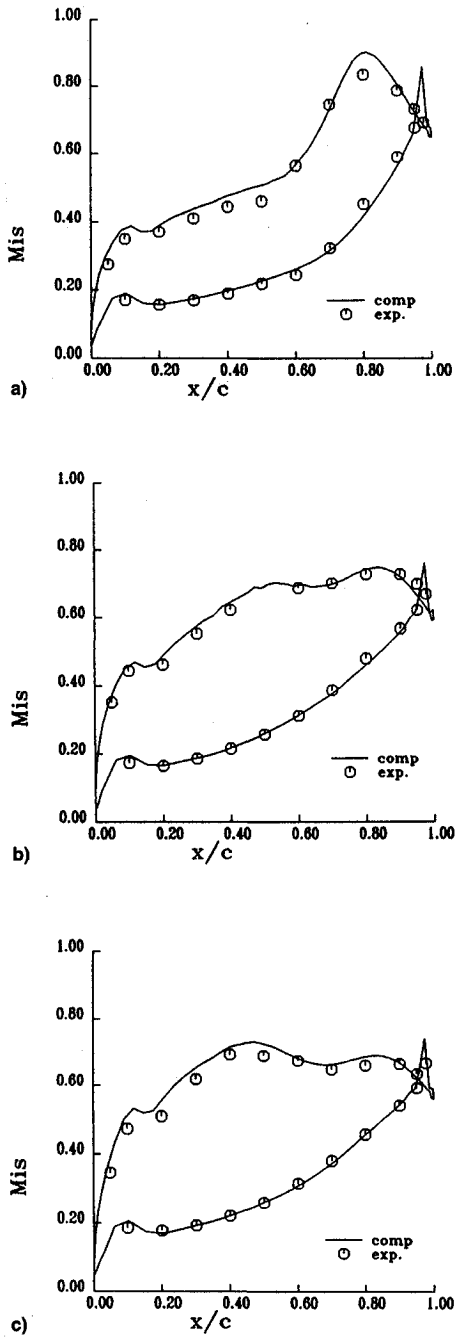

Fig. 6 Goldman annular vane with contoured end wall: a) isentropic Mach number distribution near hub, b) isentropic Mach number distribution at mid span, and c) isentropic Mach number distribution near tip.

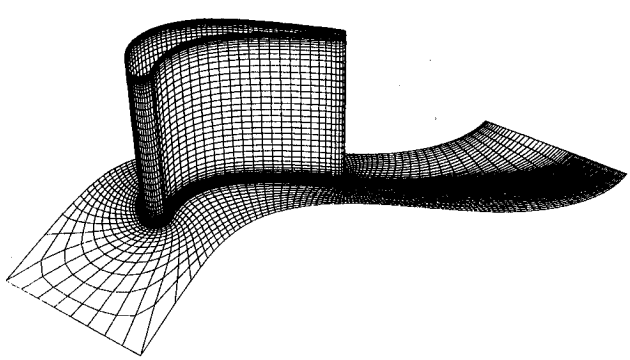

Fig. 7 177 × 33 × 65 computational grid for the Langston cascade.

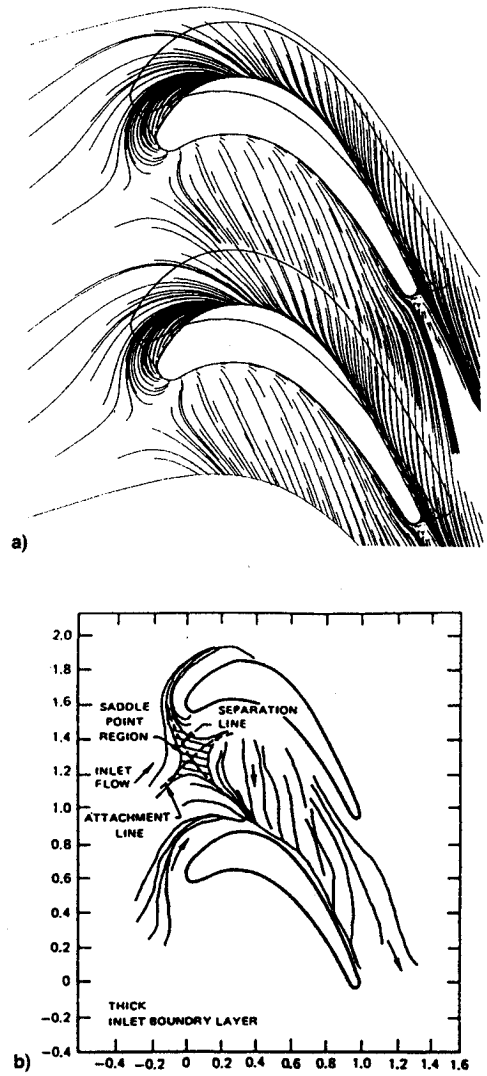

Fig. 8 Computed and experimental end wall limiting stream lines: a) computed, b) experiment.[23,24]

Even though the flow conditions of this test are at very low speed and not amenable to calculations using compressible flow codes, the Langston cascade is quite often used in three-dimensional code validation. The 177 × 33 × 65 grid we used is depicted in Fig. 7. Graziani[24] took these visualizations of the flow for two different inlet boundary-layer thicknesses. Because the aim of this study is to investigate the capability of reproducing the three-dimensional features of the flow, we are reporting calculations for the thick inlet boundary layer. Figure 8 compares the predicted and measured end wall limiting streamlines. The structure of the flow, as well as the position of the saddle point, are in good agreement with experiments. The fact that the computed saddle point is ahead of the experiment is common to several calculations (i.e., Refs. 5 and 7). In our opinion this discrepancy can be partially attributed to the difficulty of having very similar inlet boundary layers in the calculations as in the experiments. The inlet boundary layer has been modeled by simply imposing the thickness and using the $\frac{1}{7}$ power law. In addition, the experiments were made using four blades and tailboards to simulate periodicity. This slightly influences exit angle, pressure, and probably also details of secondary flows.

On the suction surface of the airfoil, the particle traces of Fig. 9 and the experimental limiting streamlines clearly demonstrate the code's capability in predicting the three-dimensional flow separation.

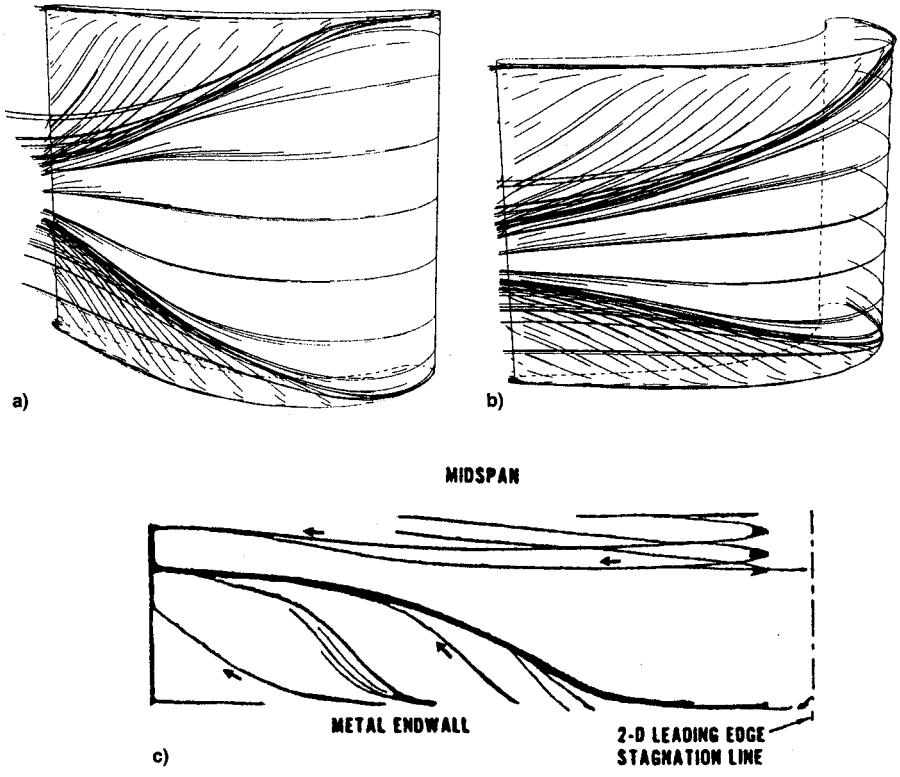

Fig. 9 Langston cascade. Computed and experimental limiting stream lines on suction side: a) computed, b) computed, and c) experiment.[23,24]

Conclusions

The central-difference, finite volume scheme with eigenvalue scaling for artificial dissipation terms, variable-coefficient implicit smoothing, and full multigrid has been extended to predict three-dimensional viscous cascade flows. We report the comparisons of calculations with experiments for the Goldman[21,22] annular cascade with and without end wall contouring, and for the Langston[23,24] cascade. For the cases studied, good overall predictions can be obtained with the Baldwin-Lomax[12] turbulence model both in terms of pressure distribution and loss coefficients. The grid-dependency study has also been conducted to determinate the grid spacing necessary to capture fine details of the three-dimensional viscous flows. With these accelerating strategies, detailed three-dimensional viscous solutions can be obtained for a reasonable fine grid in less than 1 h on a modern supercomputer.

Acknowledgments

A. Arnone would like to express his gratitude to ICOMP and NASA for providing support, facilities, and computer time for this work. Thanks are also due to Eli Turkel for useful discussions on extending the scheme to be three-dimensional. Further thanks are due to Sergio S. Stecco of the University of Florence for encouraging this work.

References

[1]Chima, R. V., and Yokota, J. W., "Numerical Analysis of Three-Dimensional Viscous Internal Flows," NASA TM 100878, July 1988.

[2]Weber, K. F., and Delaney, R. A., "Viscous Analysis of Three-Dimensional Turbomachinery Flows on Body Conforming Grids Using an Implicit Solver," American Society of Mechanical Engineers Paper 91-GT-205, June 1991.

[3]Hah, C., "Numerical Study of Three-Dimensional Flow and Heat Transfer near the Endwall of a Turbine Blade Row," AIAA Paper 89-1689, June 1989.

[4]Nakahashi, K., Nozaki, O., Kikuchi, K., and Tamura, A., "Navier-Stokes Computations of Two- and Three-Dimensional Cascade Flowfields," *Journal of Propulsion and Power*, Vol. 5, No. 3, 1989, pp. 320–326.

[5]Choi, D., and Knight, C. J., "Computation of Three-Dimensional Viscous Liner Cascade Flows," *AIAA Journal*, Vol. 26, No. 12, 1988, pp. 1477–1482.

[6]Dawes, N. W., "The Simulation of Three-Dimensional Viscous Flow in Turbomachinery Geometries Using a Solution-Adaptive Unstructured Mesh Methodology," American Society of Mechanical Engineers Paper 91-GT-124, June 1991.

[7]Subramanian, S. V., and Bozzola, R., "Numerical Simulation of Three-Dimensional Flow Fields in Turbomachinery Blade Rows Using the Compressible Navier-Stokes Equations," AIAA Paper 87-1314, June 1987.

[8]Arnone, A., and Swanson, R. C., "A Navier-Stokes Solver for Cascade Flows," NASA CR 181682, July 1988.

[9]Arnone, A., Liou, M.-S., and Povinelli, L. A., "Navier-Stokes Solution of Transonic Cascade Flow Using Non-Periodic C-Type Grids," *Journal of Propulsion and Power*, Vol. 8, No. 2, 1992, pp. 410–417.

[10]Martinelli, L., and Jameson, A., "Validation of a Multigrid Method for the Reynolds Averaged Equations," AIAA Paper 88-0414, Jan. 1988.

[11]Swanson, R. C., and Turkel, E., "Artificial Dissipation and Central Difference Schemes for the Euler and Navier-Stokes Equations," AIAA Paper 87-1107, June 1987.

[12]Baldwin, B. S., and Lomax, H., "Thin Layer Approximation and Algebraic Model for Separated Turbulent Flows," AIAA Paper 78-257, Jan. 1978.

[13]Jameson, A., Schmidt, W., and Turkel, E., "Numerical Solutions of the Euler Equations by Finite Volume Methods Using Runge-Kutta Time-Stepping Schemes," AIAA Paper 81-1259, June 1981.

[14]Pulliam, T. H., "Artificial Dissipation Models for the Euler Equations," *AIAA Journal*, Vol. 24, No. 12, 1986, pp. 1931–1940.

[15]Arnone, A., and Stecco, S. S., "Inviscid Cascade Flow Calculations Using a Multigrid Method," American Society of Mechanical Engineers Paper 89-GT-22, June 1989.

[16]Lerat, A., " Une Classe de Schemas aux Differences Implicites Pour les Systemes Hyperboliques de Lois de Conservation," Comptes Rendus Acad. Sciences, Paris, Vol. 288 A, No. 22, 1979.

[17]Jameson, A., "The Evolution of Computational Methods in Aerodynamics," *Journal of Applied Mechanics*, Vol. 50, No. 4b, 1983.

[18]Brandt, A., "Multi-Level Adaptive Computations in Fluid Dynamics," AIAA Paper 79-1455, June 1979.

[19]Ni, R.-H., "A Multiple-Grid Scheme for Solving the Euler Equations," AIAA Paper 81-1025, June 1981.

[20]Jameson, A., "Transonic Flow Calculations," Mechanical and Aerospace Engineering Rept. 1651, MAE Dept., Princeton Univ., Princeton, NJ, July 1983.

[21]Goldman, L. J., and Seasholtz, R., "Laser Anemometer Measurements in an Annular Cascade of Core Turbine Vanes and Comparison with Theory," NASA TP 2018, June 1982.

[22]Goldman, L. J., and Seasholtz, R., "Three Component Laser Anemometer Measurements in an Annular Cascade of Core Turbine Vanes with Contoured End Wall," NASA TP 2846, Nov. 1988.

[23]Langston, L. S., Nice, M. L., and Hooper, R. M., "Three-Dimensional Flow Within a Turbine Cascade Passage," American Society of Mechanical Engineers Paper 76-GT-50, June 1976.

[24]Graziani, R. A., Blair, M. F., Taylor, J. R., and Mayle, R. E., "An Experimental Study of Endwall and Airfoil Surface Heat Transfer in a Large Scale Turbine Blade Cascade," American Society of Mechanical Engineers Paper 79-GT-99, June 1979.